RSC Advances

PAPER

View Article Online
View Journal | View Issue

Cite this: *RSC Adv.*, 2026, **16**, 17946

Targeted elimination of CD44$^+$ prostate cancer stem cells using hyaluronic acid-coated selenium nanoparticles co-loaded with apigenin

Sinan Vicil, *[a] Riza Serttas [b] and Suat Erdogan [b]

Castration-resistant prostate cancer is sustained by CD44$^+$ prostate cancer stem cells (PCSCs), motivating targeted strategies that eliminate this resistant subpopulation. Here, we developed a CD44-targeted delivery system consisting of hyaluronic acid-coated selenium nanoparticles co-loaded with apigenin (HA-SeNP-Api) and evaluated its physicochemical performance, release behavior, and *anti*-PCSC activity. Dynamic light scattering revealed medium-dependent colloidal behavior: the hydrodynamic size in PBS (pH 7.4) increased from 169.8 nm (day 0) to 263.9 nm (72 h), remained comparatively stable in acidic PBS (pH 6.0; 223.6 to 231.8 nm), and markedly increased in PBS containing 10% FBS (192.4 to 542.5 nm). Zeta potential was strongly negative in PBS (~−27.8 mV) but decreased in acidic PBS (~−4.2 to −1.2 mV) and remained intermediate in PBS containing 10% FBS (~−12.1 to −13.5 mV), consistent with medium-driven charge screening. The formulation exhibited sustained apigenin release over 72 h at pH 6.0 and pH 7.4, supported by Korsmeyer–Peppas fitting of the initial phase. In CD44$^+$ PCSCs, HA-SeNP-Api produced the strongest cytotoxicity in the MTT assay (14.61% viability), exceeding the effects of apigenin, enzalutamide, SeNP, and non-targeted SeNP-Api (HA$^-$). Flow cytometry confirmed pronounced apoptosis (71.67% total apoptosis) and a marked G_2/M arrest (20.59%). Consistently, HA-SeNP-Api upregulated pro-apoptotic markers (BAX, CASP3, CASP8), reduced BCL2 expression, and suppressed pluripotency-associated genes (SOX2, OCT3/4, NANOG). Intracellular ROS profiling further indicated redox modulation by SeNP-containing formulations, with partial attenuation by NAC, supporting a ROS-linked contribution to the observed apoptotic response. Collectively, HA-SeNP-Api integrates CD44-mediated targeting with redox-driven stress signaling to achieve potent *anti*-PCSC activity, supporting further preclinical evaluation.

Received 1st December 2025
Accepted 26th March 2026

DOI: 10.1039/d5ra09291d

rsc.li/rsc-advances

Introduction

Prostate cancer is one of the leading causes of morbidity and mortality in men and, according to GLOBOCAN 2022 data, ranks second in incidence and fifth in cancer-related deaths among men, accounting for approximately 7.3% of cancer mortality.[1] Its clinical course is heterogeneous; while high survival rates can be achieved in localized disease with surgery, radiotherapy, and hormonal therapies, the 5 year survival rate drops to ~30% in advanced and metastatic stages. In addition, systemic toxicity associated with standard treatments (chemotherapy, radiotherapy, *etc.*) and the development of drug resistance significantly limit therapeutic success.[2] This situation underscores the need for more selective and safer treatment strategies, particularly those that can target resistant cell populations.

Androgen deprivation therapy is the mainstay of prostate cancer treatment; however, most cases eventually progress to castration resistance.[3] Cancer stem cells (CSCs), which possess self-renewal and tumor-initiating capacity and are resistant to conventional therapies, play a critical role in this resistance and in disease recurrence. CD44 is a characteristic surface marker of this stem cell subpopulation in prostate cancer, and CD44$^+$ cells have been shown to exhibit enhanced tumor-initiating and metastatic potential.[4] Hyaluronic acid (HA), the natural ligand of CD44, is a suitable tool for the selective targeting of CD44-overexpressing cells, and HA-coated nanocarriers have been reported to bind specifically to these cells and enhance the cellular uptake of therapeutic agents.[5] This property provides the conceptual basis for the HA-coated, CD44-targeted nanosystem designed in our study.

Nanotechnology-based drug delivery systems, owing to their controllable particle size, large surface area, and easily functionalizable structures, can improve the pharmacokinetic properties of conventional chemotherapeutics, enhance bioavailability and selective accumulation in tumor tissue, and enable controlled release and combination therapies.[6] In this

[a]*Tekirdag Namik Kemal University, Faculty of Veterinary Medicine, Department of Biochemistry, Tekirdag, Turkiye. E-mail: svicil@nku.edu.tr*
[b]*Trakya University, School of Medicine, Department of Medical Biology, Edirne, Turkiye*

way, systemic toxicity can be reduced while resistant cell populations are more effectively targeted.

The plant-derived flavonoid apigenin is a multifunctional anticancer agent that suppresses cell proliferation, enhances apoptosis, and reduces invasion/metastasis in many tumor models, including prostate cancer.[7] In $CD44^+$ prostate cancer stem cells (PCSCs), apigenin has been shown to inhibit PI3K/Akt and NF-κB signaling pathways, arrest the cell cycle in the G_0/G_1 phase, reduce migration, and activate both intrinsic and extrinsic apoptotic mechanisms.[7] Its antitumor efficacy in other cancer models through the suppression of oncogenic pathways such as Wnt/β-catenin, JAK/STAT3, and Akt further highlights apigenin as a multi-target signaling modulator.[8] However, the low aqueous solubility of apigenin ($\sim$2 μg mL^{-1}), its poor oral bioavailability, and nonspecific tissue distribution severely limit its direct clinical use.[9] Consequently, nanocarrier-based strategies have been developed for apigenin, and it has been demonstrated that liposomal systems, polymeric nanoparticles, metal nanoparticles, and targeted nanostructures can improve its solubility, stability, and tumor accumulation.[10]

Selenium is an essential trace element that regulates redox balance *via* selenoproteins and antioxidant defense systems and also possesses anticancer potential. Low selenium levels have been associated with an increased risk of prostate cancer; moreover, nano-selenium (SeNP) formulations have been shown to provide higher bioavailability and markedly lower toxicity compared with classical selenium compounds.[11] SeNPs have been reported to suppress proliferation in various cancer cell lines, induce apoptosis through modulation of reactive oxygen species (ROS) and mitochondrial pathways, and serve as suitable cores for targeted delivery platforms aimed at overcoming multidrug resistance.[12] In the context of prostate cancer, SeNPs are particularly important because they can inhibit the transcriptional activity and protein levels of the androgen receptor (AR), suppressing AR signaling *via* Akt/MDM2-mediated phosphorylation and proteasomal degradation.[13] This mechanism directly influences castration resistance and hormone-dependent growth, positioning SeNPs as strong candidates for use in combination with, or as adjuncts to, AR-targeted therapies.

Considering together the anticancer profile of apigenin, which suppresses multiple oncogenic pathways, the ability of nano-selenium (SeNP) to weaken AR signaling with a favorable toxicity profile, and the capacity of HA to selectively bind $CD44^+$ cells, integrating these three components into a single targeted nano-platform offers a rational and innovative strategy to simultaneously target both differentiated tumor cells and PCSCs responsible for treatment resistance. In this context, we designed a nanotherapeutic system (HA-SeNP-Api) in which apigenin (Api) was loaded onto HA-coated nano-selenium with CD44-mediated targeting capability, and we investigated its biological effects on $CD44^+$ PCSCs. In this study, we hypothesized that HA-coated nanoparticles co-loaded with Api and nano-selenium would effectively inhibit $CD44^+$ PCSCs by enhancing apoptosis and suppressing oncogenic signaling pathways.

Materials and methods

Cell culture

The human prostate cancer cell line LNCaP was obtained from the American Type Culture Collection (ATCC, Manassas, VA, USA). Cells were cultured in DMEM/F-12 (1 : 1) medium (Capricorn, Germany) supplemented with 10% fetal bovine serum (FBS; Gibco, USA), 1% penicillin-streptomycin (100 U mL^{-1}; Gibco, USA), 2 mM L-glutamine, and 1500 mg L^{-1} sodium bicarbonate. Cultures were maintained at 37 °C in a humidified incubator with 5% CO_2. Cells were routinely monitored for morphology and viability and were passaged at 70–80% confluency.

Enrichment of the $CD44^+$ cell subpopulation

$CD44^+$ subpopulations were isolated from LNCaP cells using a magnetic-activated cell sorting (MACS) system. Cells were labeled with CD44-PE-conjugated magnetic microbeads (Miltenyi Biotec, Germany) and passed through MACS columns according to the manufacturer's instructions. The resulting $CD44^+$ cells were transferred into serum-free DMEM/F-12 medium and cultured in suspension in the presence of 10 ng mL^{-1} leukemia inhibitory factor (LIF; Miltenyi Biotec) to maintain their stem cell properties.

Nanoparticle synthesis

For the synthesis of apigenin-loaded HA-SeNPs, a partially modified version of the methods described by Bai *et al.* (2017) and Gangadoo *et al.* (2017) was used.[14,15] SeNPs were synthesized *via* a reduction-based chemical method. All solutions and washing steps were prepared and performed using ultrapure water (18.2 MΩ cm). For synthesis, 10 mM sodium selenite (Na_2SeO_3; SS; Aromel Kimya, Türkiye) and 13 mM L-ascorbic acid (AA; Bio Basic, Canada) solutions were mixed in equal volumes (10 mL + 10 mL). The mixture was heated at 45 °C under continuous magnetic stirring for the first hour. To stabilize the reduction process, 50 μL polysorbate 20 (PS20; Sigma-Aldrich) was added after the first hour, and the mixture was further maintained at 45 °C with stirring for a total of 4 hours. Subsequently, heating was stopped, and stirring was continued at room temperature for 20 hours to obtain the nanoselenium (SeNP) stock.

Apigenin (Sigma-Aldrich, USA) and enzalutamide (Cayman, USA) were dissolved in 100% DMSO to prepare a stock solution and stored at −20 °C. A volume of 943 μL from the SeNP stock solution was mixed with 4057 μL of ultrapure water, and 6.25 μL of 50 mM apigenin solution was added. The mixture was adjusted to final concentrations of 1.0 mM SS, 1.25 mM AA, and 62.5 μM apigenin and stirred at room temperature for 24 hours. For nanoparticle surface coating, hyaluronic acid (HA; 1.5–1.8 MDa, Bugamed, Türkiye) was prepared as a solution and added dropwise (250 μL, 0.1% w/v) to the mixture, which was then stirred for an additional 24 hours.

To remove non-encapsulated apigenin and prepare fractions for analysis, an Amicon® Ultra-4 centrifugal filter unit with a 30 kDa MWCO (Merck Millipore, UFC803008, Ultracel-RC) was

used. The membrane was pre-rinsed with water according to the manufacturer's instructions (4000 × *g*, 10 min). A total of 4 mL of the nanoparticle suspension was added to the upper chamber and centrifuged at 4000 × *g* until approximately 0.5–1 mL remained in the retentate. Then, 3 mL of ultrapure water was added to the retentate, and two rounds of diafiltration were performed. The suspension remaining in the upper chamber was designated as the "NP (retentate) fraction," while all filtrates were pooled and referred to as the "free (filtrate) fraction" for LC-MS/MS analysis.

Nanoparticle characterization

The physicochemical properties of the nanoparticles were characterized by dynamic light scattering (DLS), zeta potential (ζ-potential) measurement, Fourier transform infrared spectroscopy (FTIR) and scanning electron microscopy (SEM). DLS analyses to determine hydrodynamic diameter and polydispersity index (PDI) were performed using a Zetasizer Nano ZS (Malvern Instruments, UK). Zeta potential measurements were carried out on the same instrument by the electrophoretic mobility method. DLS and ζ-potential data were acquired and processed using Zetasizer Software. For each sample, three consecutive measurements were recorded at 25 °C and reported as the mean ± SD of intensity-weighted size distributions. No additional smoothing or data manipulation beyond the default software settings was applied. FTIR spectra were recorded with a Spectrum FTIR spectrometer (Bruker, Vertex 70 ATR) in the range of 4000–400 cm^{-1} to confirm chemical bonds and surface modifications. SEM imaging was performed using JEOL JSM-7100 F and FEI QUANTA FEG 250 instruments to evaluate nanoparticle morphology and size distribution.

In vitro release profile of apigenin

The release behavior of apigenin from HA-SeNP-Api was investigated using the dialysis bag diffusion method at 37 °C under gentle shaking. To preserve sink conditions during the experiment, the release media were supplemented with Tween 80 (0.2%, v/v). Nanoparticle suspension containing a known amount of apigenin was sealed in a 10 kDa molecular weight cut-off (MWCO) dialysis membrane and immersed in release media including PBS (pH 7.4), PBS adjusted to pH 6.0, and PBS containing 10% FBS. At predetermined intervals, samples were collected from the external medium and replaced with the same volume of fresh prewarmed medium containing Tween 80. Released apigenin was quantified at 332 nm using a calibration curve prepared in the corresponding release medium, and cumulative release was expressed as the percentage of the initially loaded drug. Data were reported as mean ± SD ($n = 3$) and analyzed using the Korsmeyer–Peppas equation.

Cytotoxicity analysis (MTT assay)

The effects of apigenin, enzalutamide (Enza), SeNP, non-targeted SeNP-Api (HA^-), and the HA-SeNP-Api combination on cell viability were evaluated using the MTT assay. $CD44^+$ LNCaP cells were seeded into 96-well plates at a density of 1×10^4 cells per well and incubated for 24 h. Cells were then treated for 72 h in culture medium with the following agents: Enza (6.25 μM), apigenin (6.25 μM), SeNP (100 μM), SeNP-Api (HA^-; a combination containing SeNP 100 μM and apigenin 6.25 μM without HA coating), and HA-SeNP-Api (a combination containing SeNP 100 μM, apigenin 6.25 μM, and HA). Apigenin and enzalutamide stock solutions were prepared in DMSO, and the final DMSO concentration in the culture medium did not exceed 0.1% in any treatment group. Control wells received the corresponding volume of vehicle. Each group was tested in triplicate and repeated in three independent biological experiments. At the end of incubation, the medium was removed, cells were washed with PBS, and 1 mg mL^{-1} MTT solution (Sigma) was added to each well. After 3 h of incubation, formazan crystals were dissolved in DMSO, and absorbance was measured at 570 nm using a Multiskan GO microplate reader (Thermo Fisher). Cell viability was calculated according to the following formula: viability (%) = (OD_sample/OD_control) × 100.

Measurement of intracellular ROS

Intracellular ROS production was determined using 2′,7′-dichlorofluorescin diacetate (DCFH-DA) (Chemodex, Switzerland; Product No. D0064; CAS No. 4091-99-0). $CD44^+$ prostate cancer stem cells were cultured in 96-well plates and treated with SeNP or HA-SeNP-Api for 4 h. For ROS rescue experiments, cells were pretreated with 5 mM NAC for 45 min, washed with PBS, and then exposed to HA-SeNP-Api. NAC-alone wells received NAC pretreatment followed by fresh medium only. As a positive control, cells were treated with 300 μM H_2O_2 for 30 min. At the end of the incubation period, cells were washed and stained with 10 μM DCFH-DA in serum-free, phenol red-free medium for 30 min at 37 °C in the dark. After washing, fluorescence images were obtained immediately using a fluorescence microscope equipped with a FITC/GFP filter set under identical acquisition settings for all groups. ROS generation was interpreted according to relative fluorescence intensity.

Apoptosis analysis (Annexin V/PI)

Apoptosis levels were determined using Annexin V-FITC/propidium iodide (PI) staining. $CD44^+$ LNCaP cells were seeded into 6-well plates at a density of 2.5×10^5 cells/well and treated with the indicated agents for 72 hours. After treatment, cells were trypsinized, washed twice with cold PBS, and resuspended in Annexin binding buffer. Cells were incubated with Annexin V-FITC for 15 minutes in the dark, followed by PI staining, and analyzed using a BD FACS Calibur flow cytometer. Total apoptosis was calculated as the sum of early and late apoptotic cell populations.

Cell cycle analysis

Cell cycle distribution was assessed using PI staining. $CD44^+$ LNCaP cells were seeded into 6-well plates and treated with the test agents for 72 hours. Harvested cells were fixed overnight in 70% ethanol at 4 °C, then resuspended in PBS containing RNase A (100 μg mL^{-1}) and PI (50 μg mL^{-1}) and incubated for 30 minutes in the dark. Analyses were performed using a BD FACS

Calibur flow cytometer, and cell cycle phase distributions were evaluated.

RNA isolation, cDNA synthesis, and RT-qPCR

Total RNA was isolated using the EZ-10 Spin Column Total RNA Miniprep Kit (Bio Basic, Canada) according to the manufacturer's instructions. One microgram of RNA was reverse transcribed into cDNA using the OneScript Plus cDNA Synthesis Kit (Abmgood, Canada). Gene expression levels were analyzed using BlasTaq 2X qPCR MasterMix (Abmgood, Canada) on a StepOnePlus Real-Time PCR System (Applied Biosystems). Primers were synthesized by Sentegen Biotechnology (Ankara, Türkiye). GAPDH was used as the reference gene, and relative expression levels were calculated using the $2^{-\Delta\Delta C_t}$ method.[16] All reactions were performed with three technical and three biological replicates. Amplification curves and melt–curve profiles were inspected using StepOne Software (Applied Biosystems) to verify single, specific products for each primer pair. Ct values were exported without manual baseline modification beyond the default settings, and relative expression levels were calculated in Microsoft Excel and GraphPad Prism 9.0.

The forward and reverse primer sequences used for RT-qPCR are provided in Table 4.

Analysis of pluripotency and apoptosis markers

In $CD44^+$ cells, the expression levels of genes associated with pluripotency (SOX2, OCT3/4, NANOG), apoptosis (CASP3, CASP8, BAX, BCL2), and cell cycle regulation (P53, P21, P27) were determined by qPCR. Data are presented as fold change relative to the control group.

Statistical analysis

Data are presented as mean ± SD for physicochemical/analytical measurements and as mean ± SEM for cell-based biological assays, as indicated in the corresponding figure legends or table footnotes. Differences between groups were evaluated by one-way analysis of variance (ANOVA) followed by Tukey's post hoc test using GraphPad Prism 9.0 (GraphPad Software, USA). For ROS analysis, Dunnett's multiple comparisons test *versus* the control group was applied, as specified in the figure legend. A p value < 0.05 was considered statistically significant.

Results

To characterize the final HA-SeNP-Api formulation, hydrodynamic size, polydispersity index (PDI), and zeta potential were evaluated by dynamic light scattering under different medium conditions, followed by FTIR, SEM, and LC-MS/MS analyses.

Fourier transform infrared (FTIR) spectroscopy was employed to investigate the interactions among apigenin, hyaluronic acid, and selenium nanoparticles. The FTIR spectrum of apigenin showed characteristic bands at 3397 cm^{-1} corresponding to O–H stretching vibrations, 1655 cm^{-1} assigned to C═O/C═C stretching within the flavonoid structure, and 1016 cm^{-1} related to C–O stretching. Hyaluronic acid exhibited

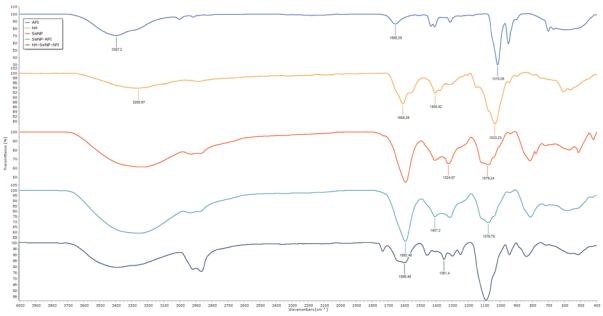

Fig. 1 FTIR spectra of apigenin (API), hyaluronic acid (HA), selenium nanoparticles (SeNP), SeNP-API, and HA-SeNP-API nanostructures. Characteristic bands of API and HA were observed, while the shift of the API band from ~1655 cm^{-1} to ~1591–1598 cm^{-1} in SeNP-API and HA-SeNP-API indicates interaction between apigenin and selenium nanoparticles and confirms the formation of the HA-coated nanostructure.

typical absorption peaks at 3259 cm^{-1} associated with O–H stretching, 1608 cm^{-1} and 1405 cm^{-1} corresponding to asymmetric and symmetric stretching of carboxylate (COO^-) groups, and 1033 cm^{-1} attributed to C–O–C stretching vibrations of the polysaccharide backbone. In the spectrum of SeNP-API, the characteristic band of apigenin at 1655 cm^{-1} shifted to approximately 1591 cm^{-1}, suggesting interaction between apigenin and the nanoparticle surface. A similar shift was observed in the HA-SeNP-API nanocomposite, where the band appeared at approximately 1598 cm^{-1} together with additional peaks at 1351 cm^{-1} and 1076 cm^{-1} associated with HA functional groups. These spectral changes indicate the successful association of apigenin with selenium nanoparticles and confirm the formation of the HA-coated SeNP-API nanostructure (Fig. 1).

SEM analysis showed that the nanoparticles were predominantly spherical to near-spherical in morphology, with individual particle diameters generally falling within the sub-200 nm range (Fig. 2). In higher-magnification images, several particles appeared to be approximately 120–155 nm in diameter, consistent with nanoscale formation. However, the particles were not completely isolated, and small clustered/aggregated assemblies were also observed. The smaller sizes observed by SEM compared with DLS were expected, since SEM

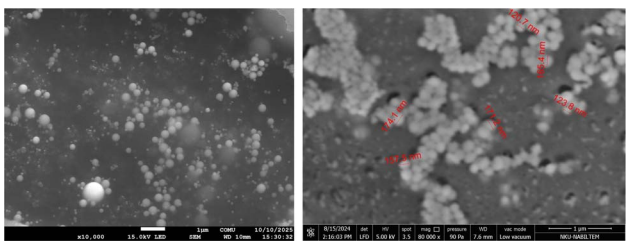

Fig. 2 SEM images of SeNP-Api and HA-SeNP-Api nanoparticles. (A) SeNP-Api nanoparticles before HA coating, showing predominantly spherical particles with a polydisperse distribution and partial aggregation. (B) HA-SeNP-Api nanoparticles at higher magnification, revealing nanoscale spherical/subspherical particles forming small clustered assemblies.

Table 1 Hydrodynamic size, polydispersity index, and zeta potential of HA-SeNP-Api in PBS (pH 7.4), acidic PBS (pH 6.0), and PBS containing 10% FBS at 0 h and after 72 h incubation. Values are presented as mean ± SD ($n = 3$)

Condition	Size (*Z*-average, nm)	PDI	Mean ζ (mV)
0 h, PBS (pH 7.4)	169.80 ± 4.45	0.45 ± 0.02	−27.8 ± 0.8
0 h, acidic PBS (pH 6.0)	223.60 ± 5.21	0.25 ± 0.01	−4.2 ± 0.9
0 h, PBS + 10% FBS	192.40 ± 3.75	0.32 ± 0.02	−12.1 ± 0.8
72 h PBS (pH 7.4)	263.90 ± 3.72	0.45 ± 0.02	−26.83 ± 1.40
72 h acidic PBS (pH 6.0)	231.80 ± 3.97	0.54 ± 0.02	−1.2 ± 1.08
72 h PBS + 10% FBS	542.50 ± 32.00	0.51 ± 0.02	−13.5 ± 1.1

reflects the dry-state core dimensions, whereas DLS measures the hydrodynamic diameter including the hydration shell, HA coating, and contributions from small aggregates (Table 1).

Dynamic light scattering analysis showed that the colloidal properties of HA-SeNP-Api were strongly influenced by the surrounding medium and incubation time (Table 1). At day 0, the formulation exhibited a *Z*-average of 169.80 ± 4.45 nm in PBS (pH 7.4), 223.60 ± 5.21 nm in acidic PBS (pH 6.0), and 192.40 ± 3.75 nm in serum. After 72 h, particle size increased to 263.90 ± 3.72 nm in PBS and 542.50 ± 32.00 nm in serum, whereas a more limited increase was observed in acidic PBS (231.80 ± 3.97 nm). The PDI was 0.45 ± 0.02 in PBS at both time points, while it increased from 0.25 ± 0.01 to 0.54 ± 0.02 in acidic PBS and from 0.32 ± 0.02 to 0.51 ± 0.02 in serum from day 0 to 72 h.

Zeta potential measurements revealed that the formulation retained a markedly negative surface charge in PBS at both day 0 and 72 h (−27.8 ± 0.8 and −26.83 ± 1.40 mV, respectively). In contrast, the absolute zeta potential decreased substantially in acidic PBS (−4.2 ± 0.9 at day 0; −1.2 ± 1.08 mV at 72 h) and remained intermediate in serum (−12.1 ± 0.8 at day 0; −13.5 ± 1.1 mV at 72 h). These findings indicate that the HA-SeNP-Api formulation was comparatively more stable in PBS, whereas serum promoted marked size enlargement and acidic conditions reduced electrostatic surface charge.

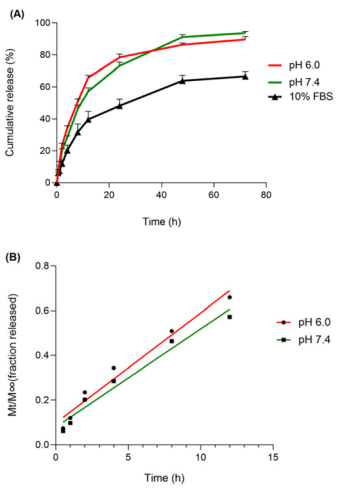

Fig. 3 Release profile of apigenin from HA-coated selenium nanoparticles in acidic PBS (ph 6.0), pbs (ph 7.4), and PBS containing 10% FBS. (A) Cumulative drug release over 72 h, showing an initial burst release followed by sustained release under all tested conditions. (B) Korsmeyer–Peppas model fitting applied to the initial release phase (0–12 h) for the ph 6.0 and ph 7.4 groups, indicating diffusion-controlled release behavior. Data are presented as mean ± SD ($n = 3$).

The release profile exhibited an initial burst release followed by a sustained release phase. In buffer conditions, cumulative apigenin release reached approximately 89–93% within 72 h, whereas the PBS containing 10% FBS group showed a slower release pattern, reaching approximately 66–67% at the final time point. The Korsmeyer–Peppas fitting of the early release stage (0–12 h) suggested that apigenin release in the buffer groups was mainly governed by diffusion through the HA-coated nanoparticle matrix. Overall, the release behavior across PBS (pH 7.4), acidic PBS (pH 6.0), and PBS containing 10% FBS indicates that the HA coating preserves structural integrity while allowing medium-dependent apigenin release under different extracellular conditions (Fig. 3).

Loading efficiency (EE%) determined by LC-MS/MS

Apigenin quantification was performed by LC-MS/MS in ESI (+)-MRM mode using water/0.2% formic acid and acetonitrile/0.2% formic acid as mobile phases, with a 12 minutes gradient and a flow rate of 0.30 mL min^{-1} (Supelco 100 × 3 mm, 2.7 μm). Concentrations were calculated by external calibration, and the amount of apigenin in each fraction was obtained using the relationship $C \times V \times D_F$. Loading efficiency was calculated using the formula: EE (%) = [apigenin in the NP fraction/(apigenin in NP fraction + apigenin in free fraction)] × 100 and was found to be 94.2%.

Cytotoxicity results

Cell viability was assessed by MTT assay, and Tukey's multiple comparison test revealed that the HA-SeNP-Api nanosystem significantly reduced viability in $CD44^+$ prostate cancer stem cells, decreasing cell viability to 14.6%, corresponding to an approximately 85.4% reduction compared with the control group ($p < 0.0001$). Among the single-agent treatments, apigenin and enzalutamide induced moderate decreases in viability (44.7% and 43.7%, respectively), whereas nanoselenium alone reduced viability by approximately 76.0%. The SeNP-Api formulation lacking HA coating produced a comparable cytotoxic effect (~78.1% reduction), indicating that the addition of apigenin to SeNP without HA targeting does not markedly enhance cytotoxicity. In contrast, HA functionalization further

Table 2 Annexin V/PI flow cytometry analysis of apoptosis in CD44$^+$ prostate cancer stem cells. HA-SeNP-Api markedly increased late apoptosis (UR) and total apoptosis (LR + UR) compared with the control group

Group	Live cells (% LL)	Early apoptosis (% LR)	Late apoptosis (% UR)	Total apoptosis (% LR + UR)
Control	99.97	0.03	0.00	0.03
Api	84.33	8.98	6.57	15.55
Enza	70.77	10.33	17.85	28.18
SeNP	42.07	4.83	49.66	54.49
HA-SeNP-Api	27.29	4.38	67.29	71.67

potentiated the antitumor activity, leading to the lowest viability observed among all treatment groups (Fig. 4).

Apoptosis analysis results

In CD44$^+$ PCSCs, HA-SeNP-Api reduced the proportion of viable cells to 27%, while increasing late apoptotic cells to 67% and total apoptosis to 72%. These values are markedly higher than those obtained with nanoselenium alone (~55% total apoptosis) and with other single agents. In Annexin V–PI flow cytometry analysis, the HA-SeNP-Api group showed 4.38% early apoptosis and 67.29% late apoptosis, yielding a total apoptotic cell fraction of 71.67%. This value was significantly higher than the total apoptotic rate of 0.03% observed in the control group ($p < 0.0001$). Total apoptosis rates were 54.49% in the SeNP group, 15.55% in the apigenin group, and 28.18% in the enzalutamide group (Table 2 and Fig. 5).

Cell cycle analysis results

In the cell cycle analysis, the HA-SeNP-Api combination induced an accumulation of 20.59% of cells in the G_2/M phase. The

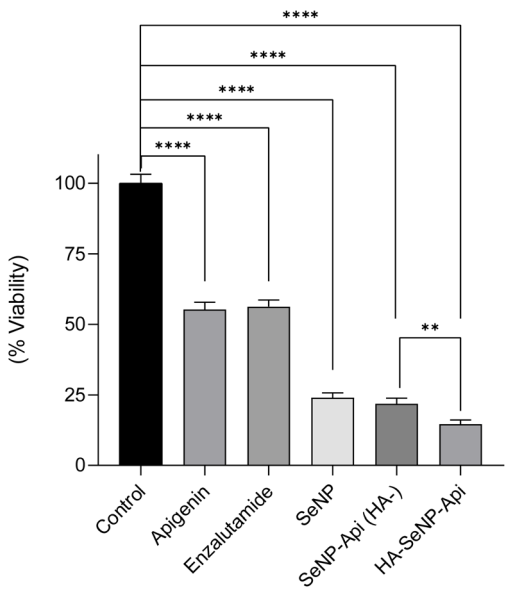

Fig. 4 Cytotoxic effects of different treatments on CD44$^+$ prostate cancer stem cells evaluated by MTT assay. The HA-SeNP-Api nanosystem produced the most pronounced reduction in cell viability, decreasing viability to ~14.6% (~85% inhibition *vs.* control) ($p < 0.0001$). Apigenin and enzalutamide alone induced moderate reductions (~55–56%), whereas nanoselenium reduced viability to ~24%. The non-targeted SeNP-Api (HA$^-$) formulation produced a comparable cytotoxic effect (~22% viability), showing no meaningful improvement over SeNP alone. These findings demonstrate that hyaluronic acid functionalization markedly enhances the antitumor activity of the nanosystem, consistent with CD44-mediated targeting of prostate cancer stem cells. Data are presented as mean ± SEM ($n = 3$). Statistical significance was determined by one-way ANOVA followed by Tukey's multiple comparison test.

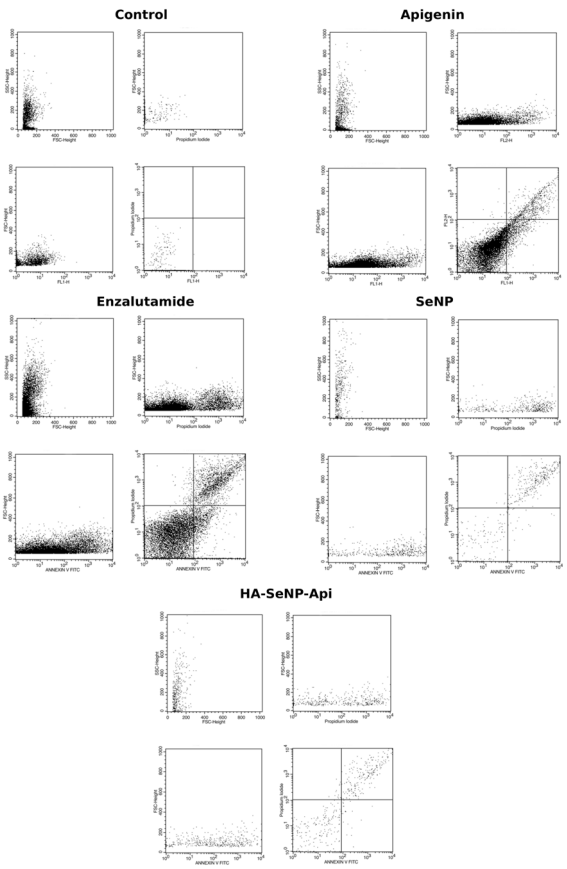

Fig. 5 Representative Annexin V/PI flow cytometry dot plots showing apoptotic changes in CD44$^+$ prostate cancer stem cells following treatment with Control, Api, Enza, SeNP, and HA-SeNP-Api. In the dot plots, the lower left quadrant (LL) indicates viable cells, the lower right quadrant (LR) early apoptotic cells, the upper right quadrant (UR) late apoptotic cells, and the upper left quadrant (UL) necrotic/dead cells. HA-SeNP-Api treatment markedly increased the apoptotic cell population compared with the control and single-treatment groups. Quantitative apoptosis results are summarized in Table 2.

Table 3 Cell-cycle distribution of $CD44^+$ prostate cancer stem cells determined by flow cytometry. HA-SeNP-Api increased the G_2/M population compared with the control group

Group	G_0/G_1 (%)	S (%)	G_2/M (%)
Control	76.58	9.52	10.86
Api	74.93	7.09	14.94
Enza	77.97	5.53	14.09
SeNP	61.57	9.30	24.22
HA-SeNP-Api	70.30	4.55	20.59

corresponding G_2/M phase ratios in the control, apigenin, enzalutamide, and SeNP groups were 10.86%, 14.94%, 14.09%, and 24.22%, respectively Table 3. In the combination group, the proportions of cells in the G_0/G_1 and S phases were 70.30% and 4.55%, respectively. In the other groups, G_0/G_1 phase distributions were 76.58% in the control, 74.93% in the apigenin group, 77.97% in the enzalutamide group, and 61.57% in the SeNP group. The percentages of cells in S phase were 9.52% (control), 7.09% (apigenin), 5.53% (enzalutamide), and 9.30% (SeNP). Overall, these results indicate that the combination treatment markedly arrests the cell cycle, particularly at the G_2/M phase (Fig. 6).

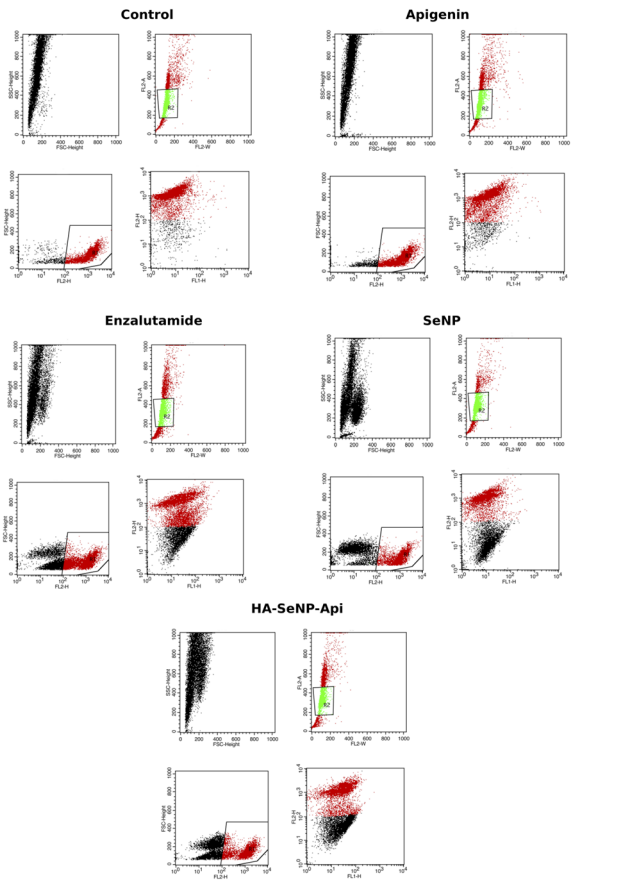

Fig. 6 Representative flow cytometric DNA-content histograms showing the cell-cycle distribution of $CD44^+$ prostate cancer stem cells after treatment with control, Api, Enza, SeNP, and HA-SeNP-Api. The proportions of cells in G_0/G_1, S, and G_2/M phases were calculated from the corresponding histograms. HA-SeNP-Api increased the proportion of cells in the G_2/M phase, consistent with cell-cycle arrest. Quantitative phase distribution data are summarized in Table 3. Data are presented as mean ± SEM ($n = 3$).

Gene expression analyses

Apoptosis- and cell cycle-related gene expression. In $CD44^+$ PCSCs, HA-SeNP-Api robustly induced apoptosis by upregulating BAX, CASP3, and CASP8 while suppressing BCL2 expression (Fig. 7). qPCR analysis showed that, in the combination group, CASP3 and CASP8 expression levels were markedly increased, whereas BCL2 expression was reduced compared with the control and single-treatment groups. In addition, HA-SeNP-Api significantly increased the expression of the cell cycle-associated genes P21 and P53, while P27 showed a modest upward trend (Fig. 8). Taken together, these findings indicate that the combined nanostructure exerts antiproliferative activity through both apoptotic induction and cell-cycle regulatory mechanisms.

Pluripotency-related gene expression. In $CD44^+$ PCSCs, HA-SeNP-Api markedly suppressed the expression of the pluripotency-associated genes NANOG, SOX2, and OCT3/4 (Fig. 9). In the combination group, NANOG, SOX2, and OCT3/4 expression levels were lower than those of the control and other treatment groups, indicating significant downregulation of stemness-related transcriptional programs. These findings suggest that HA-SeNP-Api not only promotes apoptosis and cell-cycle arrest but also suppresses the pluripotent phenotype of $CD44^+$ prostate cancer stem cells.

To evaluate the redox-modulating capacity of the formulations, intracellular reactive oxygen species (ROS) levels in $CD44^+$ PCSCs were measured using the DCFH-DA fluorescent probe (Fig. 10). Treatment with HA-SeNP-Api and SeNP alone led to a significant increase in intracellular ROS generation compared to the untreated control group ($p < 0.0001$). As expected, the positive control (H_2O_2) strongly induced ROS accumulation, while the ROS scavenger *N*-acetylcysteine (NAC) alone did not significantly alter baseline ROS levels. Notably, pretreatment with NAC partially attenuated the oxidative burst induced by HA-SeNP-Api, indicating that the nanosystem actively disrupts cellular redox homeostasis. These findings demonstrate that HA-SeNP-Api promotes an intracellular pro-oxidant state, which strongly aligns with the activation of the downstream apoptotic pathways observed in the treated $CD44^+$ cells.

Discussion

The physicochemical parameters of the HA-SeNP-Api delivery system developed in this study fall within an advantageous range when compared with apigenin-based nanocarriers reported in the literature. Under buffer conditions (PBS, pH 7.4), the formulation exhibited a hydrodynamic size of 169.80 ± 4.45 nm at day 0, increasing to 263.90 ± 3.72 nm after 72 h, indicating a moderate time-dependent enlargement while remaining within a size range compatible with nanoscale delivery. These values are comparable to the ~239 nm reported

Table 4 Forward and reverse primer sequences (5′–3′) used for quantitative real-time PCR (RT-qPCR) analysis

Gene	Forward primer (5′–3′)	Reverse primer (5′–3′)
BAX	TTGCTTCAGGGTTTCATCCA	CAGCCTTGAGCACCAGTTTG
BCL2	ATGTGTGTGGAGAGCGTCAA	ACAGTTCCACAAAGGCATCC
CASP3	GGCATTGAGACAGACAGTGG	CATGGAATCTGTTTCTTTGC
CASP8	CTGCTGGGGATGGCCACTGTG	TCGCCTCGAGGACATCGCTCTC
SOX2	GCCGAGTGGAAACTTTTGTCG	GCAGCGTGTACTTATCCTTCTT
OCT3/4	ACATGTGTAAGCTGCGGCC	GTTGTGCATAGTCGCTGCTTG
NANOG	ATGCCTCACACGGAGACTGT	AGGGCTGTCCTGAATAAGCA
P53	GAGGTTGGCTCTGACTGTACC	TCCGTCCCAGTAGATTACCAC
P21	GGCGTTTGGAGTGGTAGAAA	GACTCTCAGGGTCGAAAACG
P27	CCGGCTAACTCTGAGGACAC	TTGCAGGTCGCTTCCTTATT
GAPDH	TTGGTATCGTGGAAGGACTCA	TGTCATCATATTTGGCAGGTTT

for apigenin-loaded casein-based nanoparticles[18] and remain compatible with exploiting the enhanced permeability and retention (EPR) effect in tumor tissue. In chitosan–serum albumin–folic acid-based apigenin nanocarriers, particle sizes of ~189 nm have been reported19, while Pluronic P123/P407-based micellar systems have shown particle sizes below 100 nm[20]. In light of these data, the particle size profile of HA-SeNP-Api can be considered within an acceptable range that supports both passive (EPR) and active (CD44-mediated) targeting strategies for CD44-positive prostate cancer stem cells and tumor tissue. Notably, the formulation displayed limited size change in acidic PBS (pH 6.0) (223.60 ± 5.21 nm at day 0; 231.80 ± 3.97 nm at 72 h), whereas a pronounced increase was observed in serum (192.40 ± 3.75 nm at day 0; 542.50 ± 32.00 nm at 72 h), consistent with strong medium-dependent effects on the hydrodynamic diameter.

SEM images revealed a predominantly spherical morphology. Most individual particles were observed within the nanoscale range, typically around ~50–180 nm, although occasional larger particles and clustered structures were also detected. Considering that DLS provides the hydrodynamic diameter (including the hydration shell, HA corona, and the contribution of small aggregates), a larger DLS-derived size compared with SEM observations is expected and consistent with the literature.[17] Although some secondary clustering is visible in wide-field frames, individual nanoparticles can still be distinguished at higher magnification (Fig. 2).

The zeta potential in PBS remained markedly negative at both time points (−27.8 ± 0.8 mV at day 0; −26.83 ± 1.40 mV at

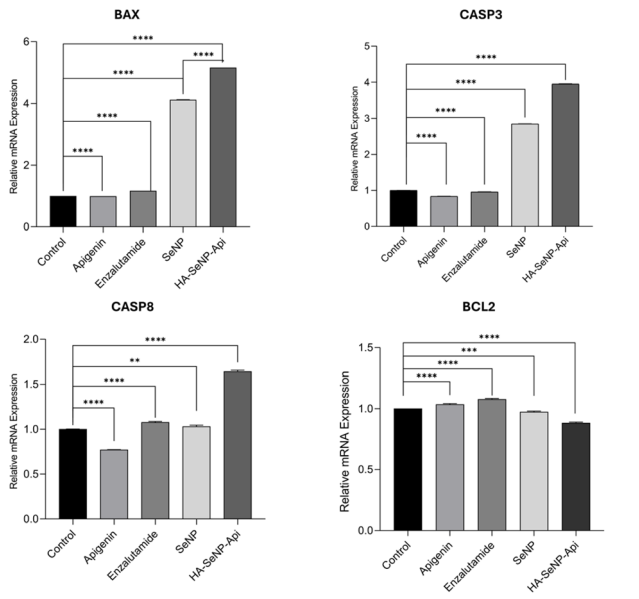

Fig. 7 Relative mRNA expression levels of apoptosis-related genes (BAX, CASP3, CASP8, and BCL2) in CD44$^+$ prostate cancer stem cells following different treatments. HA-SeNP-Api treatment markedly upregulated pro-apoptotic markers while reducing BCL2 expression, indicating activation of both intrinsic and extrinsic apoptotic pathways. Statistical significance was determined by one-way ANOVA followed by Tukey's multiple comparison test. Data are presented as mean ± SEM ($n = 3$).

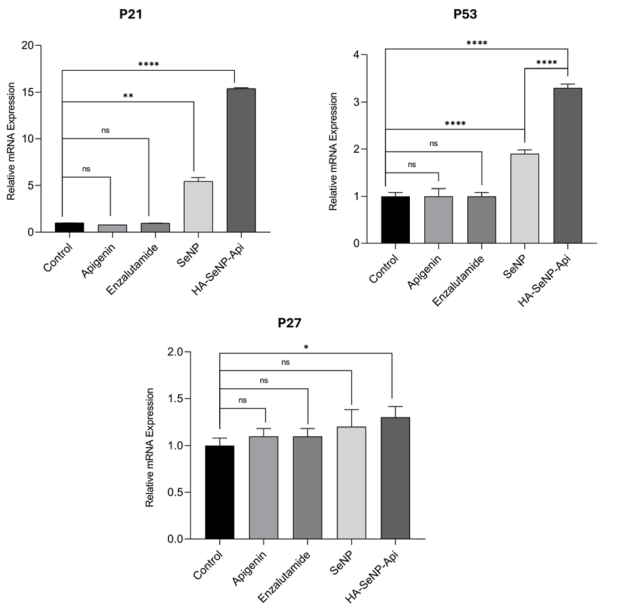

Fig. 8 Relative mRNA expression levels of cell cycle-associated genes (P21, P53, and P27) in CD44$^+$ prostate cancer stem cells following different treatments. HA-SeNP-Api markedly increased P21 and P53 expression, while P27 showed a modest increase. Data are presented as mean ± SEM ($n = 3$). Statistical significance was determined by one-way ANOVA followed by Tukey's multiple comparison test.

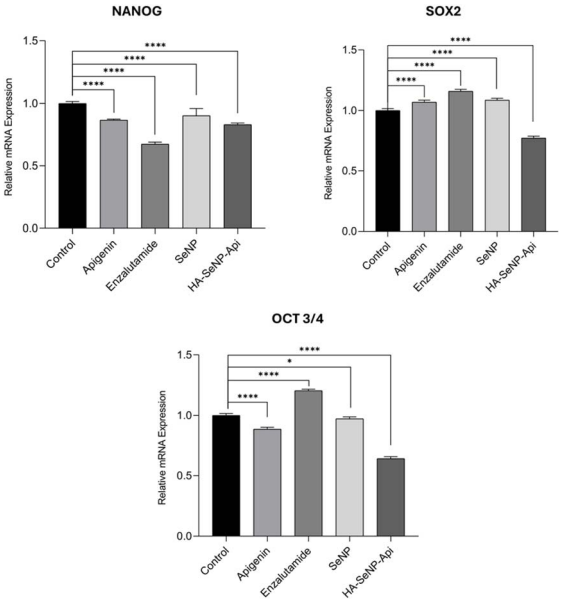

Fig. 9 Relative mRNA expression levels of pluripotency-associated genes (NANOG, SOX2, and OCT3/4) in $CD44^+$ prostate cancer stem cells following different treatments. HA-SeNP-Api suppressed the expression of NANOG, SOX2, and OCT3/4 compared with the control and other treatment groups. Data are presented as mean ± SEM (n = 3). Statistical significance was determined by one-way ANOVA followed by Tukey's multiple comparison test.

72 h), supporting electrostatic stabilization under these conditions. These values are in line with the −17 mV reported for apigenin formulations containing chitosan–serum albumin–folic acid and the −18 mV reported for Pluronic-based systems19,20 and appear more favorable in terms of colloidal stability than the lower absolute values reported for casein-based systems.18 In contrast, the absolute zeta potential decreased substantially in acidic PBS (−4.2 ± 0.9 mV at day 0; −1.2 ± 1.08 mV at 72 h) and remained intermediate under PBS containing 10% FBS conditions (−12.1 ± 0.8 mV at day 0; −13.5 ± 1.1 mV at 72 h), indicating medium-driven screening of surface charge. This negative surface charge in PBS can limit aggregation through electrostatic repulsion while preserving the conformation of the hyaluronic acid layer and thereby facilitating specific interaction with the CD44 receptor. In this way, nonspecific cellular uptake may be reduced and targeting toward CD44-positive prostate cancer stem cells enhanced. The polydispersity index values indicated a broader size distribution (PDI 0.45 ± 0.02 in PBS, increasing to 0.54 ± 0.02 in acidic PBS and 0.51 ± 0.02 under PBS containing 10% FBS conditions after 72 h), consistent with the observed medium-dependent changes in colloidal behavior. The ability to co-load apigenin and nanoselenium with high encapsulation efficiency supports a formulation design that integrates the solubility and stability advantages previously demonstrated in polymeric, protein-based, or micellar systems into a single, multicomponent, targeted platform. The slower release observed under PBS containing 10% FBS conditions compared with the buffer-only conditions may reflect protein-associated interactions at the

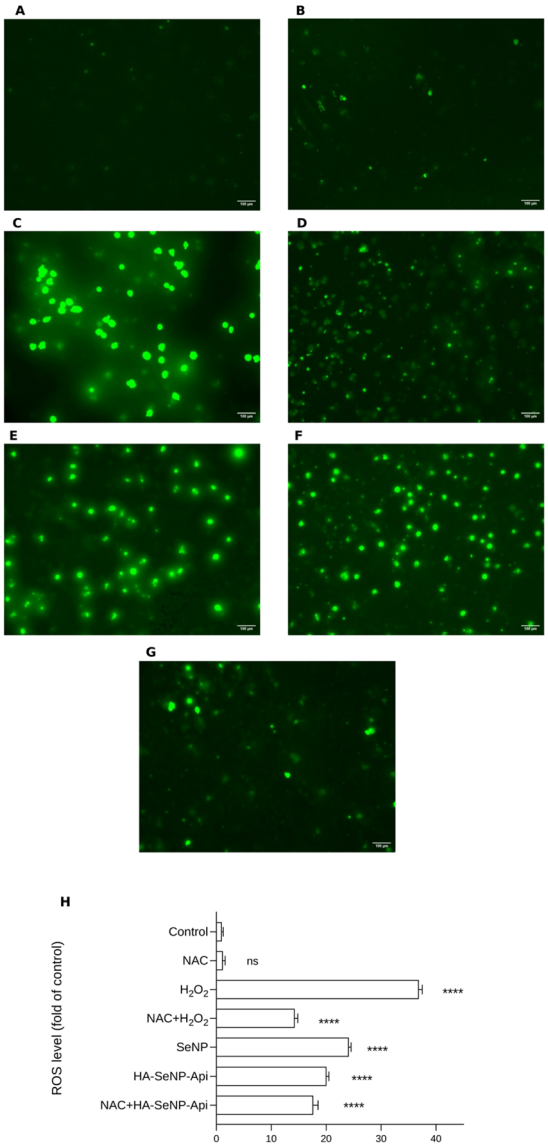

Fig. 10 Intracellular ROS generation following different treatments in $CD44^+$ prostate cancer stem cells. Representative DCFH-DA fluorescence images of (A) control, (B) NAC, (C) H_2O_2, (D) NAC + H_2O_2, (E) SeNP, (F) HA-SeNP-Api, and (G) NAC + HA-SeNP-Api groups. (H) Quantitative analysis of intracellular ROS levels expressed as fold of control. Data are presented as mean ± SD based on five imaged fields per group. Statistical analysis was performed using one-way ANOVA followed by Dunnett's multiple comparisons test *versus* the control group. ns, not significant; ****p < 0.0001. Scale bar: 100 μm.

nanoparticle interface, which could alter apigenin diffusion behavior in a biologically relevant medium.

Intracellular ROS profiling further complements the mechanistic framework of the HA-SeNP-Api formulation. DCFH-DA fluorescence imaging confirmed that the H_2O_2 group displayed a marked increase in ROS levels relative to the control, whereas NAC alone did not elicit a significant change, confirming the robustness of the experimental set-up. In this context, both SeNP and HA-SeNP-Api significantly elevated intracellular ROS compared with the control group, indicating that nanoselenium-containing formulations modulate cellular

redox homeostasis in $CD44^+$ PCSCs. Importantly, the reduction of ROS levels in the NAC + HA-SeNP-Api group suggests that the oxidative burst triggered by the nanosystem is at least partially ROS-dependent. This observation aligns with the downstream apoptosis-related findings in the present study, as increased ROS can facilitate mitochondrial dysfunction and strengthen pro-apoptotic signaling, thereby contributing to the observed Bax/Bcl-2 imbalance and caspase activation. Taken together, these results support a mechanism in which HA-SeNP-Api combines HA-mediated cellular targeting with redox-driven stress signaling, which likely contributes to its enhanced cytotoxic activity in $CD44^+$ prostate cancer stem cells. Accordingly, ROS modulation may represent an upstream event linking HA-SeNP-Api exposure to coordinated apoptotic signaling in $CD44^+$ PCSCs.

In line with these observations, the biological effects of HA-SeNP-Api are consistent with the complementary mechanisms previously described for apigenin and nanoselenium. In $CD44^+$ prostate cancer stem cells, apigenin has been reported to activate the extrinsic pathway, increase CASP8 and CASP3 expression, and trigger TNF-α-mediated caspase-dependent apoptosis, while exerting a more limited effect on components of the intrinsic pathway.[7] Nanoselenium, by contrast, has been characterized in various tumor models as an agent that triggers intrinsic apoptosis *via* the mitochondrial pathway through increased Bax, suppression of Bcl-2, cytochrome c release, and CASP3 activation, while offering a lower toxicity and higher bioavailability profile than inorganic selenite and selenate.[14,21] Selenium nanoparticles stabilized with mesoporous silica and Pluronic F68 have been shown to induce marked apoptosis in cancer cells while exhibiting low toxicity in experimental models, supporting the use of nanoselenium as a safe yet effective antitumor core.[22] Recent data further highlight selenium nanoparticles as a versatile biomedical platform through ROS modulation, immunoregulation, and anticancer effects.[23] Together, these complementary actions provide a mechanistic rationale for the enhanced apoptotic response observed with HA-SeNP-Api in $CD44^+$ PCSCs.

In this context, HA-SeNP-Api simultaneously activated both the extrinsic (*via* CASP8) and intrinsic (*via* the Bax/Bcl-2 balance and CASP3) pathways, achieving approximately a 4-fold increase in CASP3, a ∼1.6-fold increase in CASP8, and an ∼12% reduction in BCL2 expression. This bidirectional pathway activation is consistent with evidence that nanoselenium acts primarily through the intrinsic pathway, whereas apigenin acts through the extrinsic pathway, and that when combined within an appropriate nanocarrier framework they can elicit a potent apoptotic response.[14,24] A CD44-targeted nanoliposomal quercetin formulation was previously reported to induce ∼60% apoptosis in $CD44^+$ PCSCs.[25] In our study, the 71.67% apoptosis observed with HA-SeNP-Api reflects a similarly strong apoptotic response, supporting a potential synergy between nanoselenium and apigenin under hyaluronic acid-mediated CD44 targeting.

Comparable findings have been reported in other nano-apigenin systems, such as chitosan-based Ap-CH-BSA-FANPs,[19] Pluronic micelle–apigenin,[20] and apigenin nanoparticles combined with 5-FU,[26] where caspase activation, suppression of anti-apoptotic proteins, and reductions in IC_{50} values have been demonstrated.

The cytotoxicity data obtained from the MTT assay further support the enhanced therapeutic performance of the HA-SeNP-Api nanosystem. Among all treatment groups, HA-SeNP-Api produced the most pronounced reduction in $CD44^+$ prostate cancer stem cell viability, decreasing cell viability to approximately 14.6%, corresponding to an ∼85% reduction compared with the control group. In contrast, single-agent treatments with apigenin and enzalutamide resulted in moderate reductions in viability (∼55–56%), while nanoselenium alone reduced viability to approximately 24%. The SeNP-Api formulation lacking HA coating exhibited a comparable but slightly weaker cytotoxic effect (∼22% viability) relative to HA-SeNP-Api. These findings suggest that hyaluronic acid functionalization enhances the cytotoxic efficacy of the nanoparticle system, most likely by facilitating CD44-mediated cellular uptake and increasing intracellular drug accumulation in $CD44^+$ prostate cancer stem cells. The markedly stronger inhibitory effect of HA-SeNP-Api compared with the individual agents indicates that the nanosystem not only integrates the intrinsic cytotoxic mechanisms of apigenin and nanoselenium but also benefits from HA-directed targeting toward the CD44-positive cancer stem cell population.

In this context, HA-SeNP-Api can be regarded as a rational design that integrates the known pro-apoptotic effects of apigenin with the intrinsic pathway activation afforded by nanoselenium, while focusing this combined activity on PCSCs through CD44-mediated targeting.

The pronounced G_2/M phase accumulation (20.59%) observed following HA-SeNP-Api treatment indicates that the transition of DNA-replicated PCSCs into mitosis is blocked and that cell-cycle arrest is being enforced *via* the p53–P21–P27 axis. Apigenin has previously been reported to induce G1 or G_2/M arrest through p53-dependent mechanisms in various tumor models.[27] In the present study, the G_2/M arrest observed together with increased P21 and P27 expression suggests that the cell cycle-regulatory effect of apigenin is potentiated by the nanoselenium core and HA-mediated CD44 targeting. Accordingly, HA-SeNP-Api appears to elicit a robust antiproliferative response that durably suppresses the proliferation of $CD44^+$ PCSCs. The G_2/M accumulation seen with HA-SeNP-Api also implies that the nanoselenium core contributes not only to apoptosis but also actively to cell-cycle control, in agreement with the reported advantages of nano-apigenin formulations.[28]

Following HA-SeNP-Api treatment, SOX2, OCT3/4, and NANOG expression levels decreased to 0.83-, 0.64-, and 0.77-fold, respectively, indicating that the system functions not merely as a cytotoxic agent but as an "*anti*-stemness" platform that targets the self-renewal capacity and pluripotency network of PCSCs. High expression of these transcription factors has been associated with castration resistance, poor treatment response, and unfavorable prognosis.[29] Thus, their suppression can be considered critical in reducing the risk of tumor recurrence and metastatic spread. A CD44-targeted, HA-modified nanoliposomal quercetin formulation has previously been

shown to reduce the proportion of $CD44^+$ cells and decrease OCT3/4 expression.[25] The broader inhibitory effect of HA-SeNP-Api on the SOX2/OCT3/4/NANOG axis points to a stronger strategy aimed at depleting the prostate cancer stem cell pool. Given that there are limited data in the literature on the direct suppression of pluripotency markers by nanoselenium-based systems, the *anti*-stemness profile observed here allows nanoselenium to be repositioned—especially when combined with CD44 targeting—as an active component capable of modulating the stem cell-ike phenotype.

Although enzalutamide and other AR-targeted therapies initially reduce tumor burden, they are associated over time with an expansion of stem-like cell populations, overexpression of SOX2 and NANOG, and the selection of castration-resistant clones.[30] HA-SeNP-Api has the potential to eliminate this reservoir by targeting both differentiated tumor cells and the $CD44^+$ prostate cancer stem cell subpopulation, independently of AR signaling. Biogenic selenium nanoparticles have been reported to induce TNF/IRF1-mediated necroptosis in LNCaP cells, reduce AR and PSA expression, and exert selective antitumor effects.[31] These findings suggest that the nanoselenium component may help overcome enzalutamide resistance by suppressing AR-dependent pathways. The negatively charged, HA-rich surface of HA-SeNP-Api supports selective uptake by $CD44^+$ cells, thereby promoting the accumulation of therapeutic concentrations in target cells and reducing the risk of systemic toxicity.[19,25]

Studies on rosuvastatin- and Cu-SeNP-loaded PLGA/PDMS *in situ* implants and selenium–sorafenib nanocomplexes have shown that selenium nanoparticle-based combinations can enhance chemotherapeutic efficacy, improve selectivity, and enable controlled drug release.[24,32] By adapting this concept to PCSCs, HA-SeNP-Api emerges as a multifunctional therapeutic candidate that integrates the intrinsic antitumor effects of nanoselenium, the signaling-suppressive and proapoptotic properties of apigenin, and HA-mediated CD44 targeting within a single platform.

Conclusions

In summary, the CD44-targeted HA-SeNP-Api nanosystem exhibited physicochemical characteristics consistent with successfully reported apigenin nanocarriers and demonstrated medium-dependent colloidal behavior under buffer, acidic, and serum-containing conditions, together with a sustained release profile. Biologically, the nanosystem exerted a multilayered antitumor effect in $CD44^+$ prostate cancer stem cells by promoting apoptosis, inducing G_2/M phase arrest, suppressing stemness-associated gene expression, and modulating intracellular ROS levels. These findings support the view that HA-SeNP-Api functions not only as a nanoformulation with enhanced cytotoxic potential, but also as a targeted platform capable of interfering with key survival and self-renewal mechanisms in prostate cancer stem cells.

However, the present study has several limitations. First, the biological evaluation was restricted to *in vitro* experiments using $CD44^+$ PCSCs derived from a single prostate cancer cell line (LNCaP), which limits the generalizability of the findings. Second, although the inclusion of the non-targeted SeNP-Api (HA^-) group supports the contribution of HA coating, direct verification of CD44-mediated targeting specificity through receptor-blocking studies, uptake assays, or CD44-negative cell models was not performed. Third, although colloidal behavior was assessed under acidic and serum-containing conditions, further studies are needed to investigate longer-term stability and protein corona formation in biologically relevant media. In addition, the absence of *in vivo* pharmacokinetic, biodistribution, and therapeutic validation currently limits translational interpretation.

Therefore, future studies should evaluate HA-SeNP-Api in additional prostate cancer models, including androgen-independent and CD44-variable cell systems, and extend the work to *in vivo* preclinical settings. Further mechanistic studies addressing nanoparticle uptake, receptor-level targeting specificity, and serum-associated nano-bio interactions would also strengthen the translational potential of this platform. Despite these limitations, the present findings identify HA-SeNP-Api as a promising candidate for the targeted elimination of prostate cancer stem cell populations associated with therapeutic resistance and disease recurrence.

Author contributions

Sinan Vicil: conceptualization, methodology, investigation, nanoparticle synthesis, cell culture experiments, flow cytometry, formal analysis, data curation, visualization, writing – original draft. Rıza Serttas: investigation, RT-qPCR analysis, data curation, cell culture experiments, formal analysis, writing – review & editing. Suat Erdogan: conceptualization, methodology, supervision, project administration, cell culture experiments, validation, writing – review & editing. All authors have read and approved the final version of the manuscript.

Conflicts of interest

There are no conflicts to declare.

Data availability

All data supporting the findings of this study are available in the Science Data Bank repository at https://doi.org/10.57760/sciencedb.32286.

Acknowledgements

This study was funded by Scientific Research Projects Coordination Unit of Tekirdag Namik Kemal University. Project number: NKUBAP.10.GC.24.537.

Notes and references

1 F. Bray, M. Laversanne, H. Sung, J. Ferlay, R. L. Siegel, I. Soerjomataram and A. Jemal, *Ca-Cancer J. Clin.*, 2024, **74**, 229–263, DOI: 10.3322/caac.21834.

2 (*a*) R. L. Siegel, K. D. Miller, N. S. Wagle and A. Jemal, *Ca-Cancer J. Clin.*, 2023, **73**, 17–48, DOI: 10.3322/caac.21763; (*b*) H. Chen, F. Lyu and X. Gao, *Prostate Cancer Prostatic Dis.*, 2026, **29**, 36–46, DOI: 10.1038/s41391-024-00933-w.

3 P. P. Kushwaha, S. Verma, S. Kumar and S. Gupta, *Cancer Drug Resist.*, 2022, **5**, 459–471, DOI: 10.20517/cdr.2022.07.

4 F. Moltzahn and G. N. Thalmann, *Transl. Androl. Urol.*, 2013, **2**, 242–253, DOI: 10.3978/j.issn.2223-4683.2013.09.06.

5 C. Chen, S. Zhao, A. Karnad, *et al.*, *J. Hematol. Oncol.*, 2018, **11**, 64, DOI: 10.1186/s13045-018-0605-5.

6 S. Sarkar and S. Das, *Nanoscale Adv.*, 2024, **6**, 1965–1985, DOI: 10.1039/D4NA00086B.

7 S. Erdogan, O. Doganlar, Z. B. Doganlar, R. Serttas, K. Turkekul, I. Dibirdik and A. Bilir, *Life Sci.*, 2016, **162**, 77–86, DOI: 10.1016/j.lfs.2016.08.019.

8 (*a*) M. Hasnat, M. Pervin, J. H. Lim and B. O. Lim, *Molecules*, 2015, **20**, 21157–21166; (*b*) H.-S. Seo, J. K. Jo, J. M. Ku, H.-S. Choi, Y. K. Choi, J.-K. Woo, H. I. Kim, S.-Y. Kang, K. M. Lee, K. W. Nam, N. Park, B.-H. Jang, Y. C. Shin and S.-G. Ko, *Biosci. Rep.*, 2015, **35**, e00276, DOI: 10.1042/BSR20150165; (*c*) H.-H. Cao, J.-H. Chu, H.-Y. Kwan, T. Su, H. Yu, C.-Y. Cheng, X.-Q. Fu, H. Guo, T. Li, A. K.-W. Tse, G.-X. Chou, H.-B. Mo and Z.-L. Yu, *Sci. Rep.*, 2016, **6**, 21731, DOI: 10.1038/srep21731; (*d*) M. Xu, S. Wang, Y. Song, J. Yao, K. Huang and X. Zhu, *Oncol. Lett.*, 2016, **11**, 3075–3080, DOI: 10.3892/ol.2016.4331; (*e*) Z. Zhou, M. Tang, Y. Liu, Z. Zhang, R. Lu and J. Lu, *Anti-Cancer Drugs*, 2017, **28**, 446–456, DOI: 10.1097/CAD.0000000000000479.

9 (*a*) A. Waheed, S. Zameer, K. Ashrafi, A. Ali, N. Sultana, M. Aqil, Y. Sultana and Z. Iqbal, *Curr. Pharm. Des.*, 2023, **29**, 1326–1340, DOI: 10.2174/1381612829666230529164321; (*b*) V. Naponelli, M. T. Rocchetti and D. Mangieri, *Int. J. Mol. Sci.*, 2024, **25**, 5569, DOI: 10.3390/ijms25105569.

10 (*a*) M. Kazi, A. Alhajri, S. M. Alshehri, E. M. Elzayat, O. T. Al Meanazel, F. Shakeel, O. Noman, M. A. Altamimi and F. K. Alanazi, *Pharmaceutics*, 2020, **12**, 749; (*b*) M. Dobrzyńska, M. Napierała and E. Florek, *Biomolecules*, 2020, **10**, 1268, DOI: 10.3390/biom10091268; (*c*) M. Moslehi, S. Rezaei, P. Talebzadeh, *et al.*, *Clin. Exp. Pharmacol. Physiol.*, 2023, **50**, 3–18, DOI: 10.1111/1440-1681.13725; (*d*) P. Pandey, F. Khan and T. K. Upadhyay, *Chem. Biol. Drug Des.*, 2023, **101**, 1446–1458, DOI: 10.1111/cbdd.14206.

11 (*a*) A. Khurana, S. Tekula, M. A. Saifi, P. Venkatesh and C. Godugu, *Biomed. Pharmacother.*, 2019, **111**, 802–812, DOI: 10.1016/j.biopha.2018.12.146; (*b*) A. Kumar and K. S. Prasad, *J. Biotechnol.*, 2020, **325**, 152–163, DOI: 10.1016/j.jbiotec.2020.11.004; (*c*) J. Jiang, B. Chen, B. Tang and Q. Wei, *Pharmaceuticals*, 2023, **16**, 1250, DOI: 10.3390/ph16091250.

12 (*a*) T. Chen, Y. S. Wong, W. Zheng, Y. Bai and L. Huang, *Colloids Surf., B*, 2008, **67**, 26–31; (*b*) T. Liu, L. Zeng, W. Jiang, Y. Fu, W. Zheng and T. Chen, *Nanomedicine*, 2015, **11**, 947–958, DOI: 10.1016/j.nano.2015.01.009; (*c*) F. Maiyo and M. Singh, *Nanomedicine*, 2017, **12**, 1075–1089, DOI: 10.2217/nnm-2017-0024; (*d*) S. Tang, T. Wang, M. Jiang, C. Huang, C. Lai, Y. Fan and Q. Yong, *Int. J. Biol. Macromol.*, 2019, **128**, 444–451, DOI: 10.1016/j.ijbiomac.2019.01.152.

13 L. Kong, Q. Yuan, H. Zhu, Y. Li, Q. Guo, Q. Wang, X. Bi and X. Gao, *Biomaterials*, 2011, **32**, 6515–6522, DOI: 10.1016/j.biomaterials.2011.05.032.

14 K. Bai, B. Hong, Z. Hong, J. Sun and C. Wang, *J. Nanobiotechnol.*, 2017, **15**, 92, DOI: 10.1186/s12951-017-0324-z.

15 S. Gangadoo, D. Stanley, R. J. Hughes, R. J. Moore and J. Chapman, *Synth. React. Inorg. Metal-Org. Nano-Metal Chem.*, 2017, **47**, 1568–1576, DOI: 10.1080/24701556.2017.1357611.

16 K. J. Livak and T. D. Schmittgen, *Methods*, 2001, **25**, 402–408, DOI: 10.1006/meth.2001.1262.

17 Q. Tarrés, R. Aguado, J. O. Zoppe, P. Mutjé, N. Fiol and M. Delgado-Aguilar, *Nanomaterials*, 2022, **12**, 4288, DOI: 10.3390/nano12234288.

18 L. Wang, W. Jia, Q. Yang, H. Cai and X. Zhao, *Food Hydrocoll.*, 2024, **146**, 109194, DOI: 10.1016/j.foodhyd.2023.109194.

19 M. M. M. Zayed, H. A. Sahyon, N. A. N. Hanafy and M. A. N. El-Kemary, *Pharmaceutics*, 2022, **14**, 1160, DOI: 10.3390/pharmaceutics14061160.

20 A. Patra, S. Satpathy, S. Rai, P. K. Naik, M. Kazi and M. D. Hussain, *Polym. Adv. Technol.*, 2025, **36**, e70347, DOI: 10.1002/pat.70347.

21 (*a*) Y. Huang, L. He, W. Liu, C. Fan, W. Zheng, Y. S. Wong and T. Chen, *Biomaterials*, 2013, **34**, 7106–7116, DOI: 10.1016/j.biomaterials.2013.04.067; (*b*) A. Ullah, J. Mu, F. Wang, M. W. H. Chan, X. Yin, Y. Liao, Z. A. Mirani, S. Sebt-e-Hassan, S. Aslam, M. Naveed, M. N. Khan, Z. Khatoon and M. R. Kazmi, *Antioxidants*, 2022, **11**, 1916, DOI: 10.3390/antiox11101916; (*c*) S. Anjum, M. Hashim, M. Imran, S. Babur, S. Adnan, C. Hano and W. N. Ibrahim, *Cancer Rep.*, 2025, **8**, e70210, DOI: 10.1002/cnr2.70210.

22 M. Wang, X. Sun, Y. Wang, X. Deng, J. Miao, D. Zhao, K. Sun, M. Li, X. Wang, W. Sun and J. Qin, *ACS Omega*, 2022, **7**, 44851–44860, DOI: 10.1021/acsomega.2c04975.

23 K. K. Karunakar, B. V. Cheriyan, H. Shakti, *et al.*, *Biomed. Mater. & Devices*, 2025, DOI: 10.1007/s44174-025-00445-8.

24 E. G. Varlamova, V. V. Khabatova, S. V. Gudkov and E. A. Turovsky, *Int. J. Mol. Sci.*, 2023, **24**, 2411, DOI: 10.3390/ijms24032411.

25 K. Turkekul and S. Erdogan, *J. Cancer Prev.*, 2023, **28**, 160–174, DOI: 10.15430/JCP.2023.28.4.160.

26 (*a*) S. Daneshvar, M. Y. Zamanian, M. S. Ivraghi, *et al.*, *Food Sci. Nutr.*, 2023, **11**, 6789–6801; (*b*) P. Goleij, S. Ferdousmakan, M. A. K. Tabari, A. Amini, D. S. Larsen, M. Daglia, A. Javan, T. Li, H. Khan and Y. Xu, *Transl. Oncol.*, 2025, **59**, 102455, DOI: 10.1016/j.tranon.2025.102455.

27 (*a*) S. Shukla and S. Gupta, *Free Radic. Biol. Med.*, 2008, **44**, 1833–1845, DOI: 10.1016/j.freeradbiomed.2008.02.007; (*b*) S. H. Jeong, H. H. Kim, M. Y. Park, P. B. Bhosale, A. Abusaliya, C. K. Won, K. I. Park, E. Kim, J. D. Heo, H. W. Kim, M. Ahn, J. K. Seong and G. S. Kim, *Int. J. Mol. Sci.*, 2023, **24**, 9240, DOI: 10.3390/ijms24119240.

28 S. Bhattacharya, L. Mondal, B. Mukherjee, L. Dutta, I. Ehsan, M. C. Debnath, R. H. Gaonkar, M. M. Pal and S. Majumdar, *Nanomedicine*, 2018, **14**, 1905–1917, DOI: 10.1016/j.nano.2018.05.011.

29 (*a*) C. Jeter, B. Liu, X. Liu, *et al.*, *Oncogene*, 2011, **30**, 3833–3845, DOI: 10.1038/onc.2011.114; (*b*) S. Gong, Q. Li, C. R. Jeter, Q. Fan, D. G. Tang and B. Liu, *Mol. Carcinog.*, 2015, **54**, 679–687, DOI: 10.1002/mc.22340.

30 F. Yuan, W. Hankey, D. Wu, *et al.*, *Nucleic Acids Res.*, 2019, **47**, 10104–10114, DOI: 10.1093/nar/gkz790.

31 P. Sonkusre, *Front. Oncol.*, 2020, **9**, 1541, DOI: 10.3389/fonc.2019.01541.

32 A. Maged, M. Mabrouk, H. T. Nour El-Din, L. Osama, S. M. Badr-Eldin and A. A. Mahmoud, *Front. Pharmacol*, 2024, **15**, 1397639, DOI: 10.3389/fphar.2024.1397639.